Mon. Not. R. Astron. Soc. **000**, 000–000 (0000) Printed 3 December 2009 (MN LaTeX style file v2.2)

The luminosity function and the rate of *Swift*'s Gamma Ray Bursts

David Wanderman[1] and Tsvi Piran[2]

Racah Institute of Physics, The Hebrew University, Jerusalem 91904, Israel. [1]email:david.wanderman@mail.huji.ac.il [2]email:tsvi@phys.huji.ac.il

3 December 2009

ABSTRACT

We invert directly the redshift - luminosity distribution of observed long *Swift* GRBs to obtain their rate and luminosity function. Our best fit rate is described by a broken power law that rises like $(1+z)^{2.1^{+0.5}_{-0.6}}$ for $0 < z < 3$ and decrease like $(1+z)^{-1.4^{+2.4}_{-1.0}}$ for $z > 3$. This transition begins earlier and its amplitude is somewhat smaller than the corresponding transition in the SFR. The local rate is $\rho_0 \simeq 1.3^{+0.6}_{-0.7}[Gpc^{-3}yr^{-1}]$. The luminosity function is well described by a broken power law with a break at $L* \simeq 10^{52.5\pm0.2}[erg/sec]$ and with indices $\alpha = 0.2^{+0.2}_{-0.1}$ and $\beta = 1.4^{+0.3}_{-0.6}$. The recently detected GRB 090423, with redshift ≈ 8, fits nicely into the model's prediction, verifying that we are allowed to extend our results to high redshifts. For non evolving luminosity functions we can rule out a GRB rate that follows the star formation rate (SFR), unless the latter is steeply rising at large redshifts.

1 INTRODUCTION

Gamma-ray bursts (GRBs) are short and intense pulses of soft γ-rays. In this work we study their luminosity function and their cosmic rate. Knowing these functions would help us understanding the nature of GRBs and determine their progenitors. This may also shed light on the still mysterious physics of the central engine.

The luminosity function and the rate are observationally entangled as the observed rate is a convolution of the luminosity function with the cosmic rate. For this reason, almost every work before this paper must had a-priori assumptions on at least one of these functions. At first - having no motivation to belive otherwise - the rate was assumed to be constant. The simplest form for the luminosity function was a standard candle i.e. a constant luminosity. The early studies used the measured $\langle V/V_{\max}\rangle$ value to find the typical luminosity (Mao and Paczynski 1992; Piran 1992; Fenimore et al. 1993; Ulmer and Wijers 1995; Ulmer et al. 1995) and correspondingly a maximal distance from which GRBs were observed. Later, using the flux distribution ($logN - logP$ relation), Cohen and Piran (1995) and later Loredo and Wasserman (1998) showed how relaxing the standard candle assumption allows a corresponding relaxing of the constat rate or the standard candle assumptions.

Noticing that the hosts of the bursts are in star forming regions, Paczyński (1998) suggested that GRBs follow the star formation rate (SFR) (see also Totani 1997; Wijers et al. 1998a). The detection of a supernova associated with GRB980425 Galama et al. (1998), strengthened the expectation that the GRB rate should follow the star formation rate. Using this proportionality, many studies examined the typical luminosity assuming standard candles (e.g. Wijers et al. 1998a; Totani 1999), or examined more elaborated shapes of the luminosity function (e.g. Schmidt 1999, 2001b,a; Guetta et al. 2005; Firmani et al. 2004; Guetta and Piran 2005).

After the launch of the *Swift* satellite, many more GRBs afterglows were observed, and a worldwide network of observers have detected gamma-ray bursts from higher redshifts than was previously possible, sparking renewed interest in the GRB redshift distribution (e.g. Berger et al. 2005; Natarajan et al. 2005; Bromm and Loeb 2006; Jakobsson et al. 2006; Le and Dermer 2007; Yüksel and Kistler 2007; Salvaterra and Chincarini 2007; Liang et al. 2007; Chary et al. 2007). It soon became clear that the rate of GRBs does not simply follow the global star formation rate, as was believed earlier. Firmani et al. (2005); Le Floc'h et al. (2006); Daigne et al. (2006); Le and Dermer (2007); Guetta and Piran (2007) conclude that the GRB rate differs from the SFR, and we have more high redshift bursts than expected by the SFR. Yüksel et al. (2008) uses the high luminosity subsample of bursts with redshifts, which can be detected up to high redshifts, to find the GRB rate without assuming any luminosity function. They find that GRB rate to be higher on high ($z > 4$) redshifts than if it followed Hopkins and Beacom (2006) SFR. Alternatively luminosity evolution, is suggested by some authors: e.g. Lloyd-Ronning et al. (2002); Firmani et al. (2004); Matsubayashi et al. (2006); Kocevski and Liang (2006) - using variability - luminosity, and lag - luminosity relations. Salvaterra et al. (2008) used a sample of long bursts with good redshift determination and a measured peak energy, and found evidence for luminosity evolution. They compared the two scenarios: of luminosity evolution and of rate evolution over the SFR, and found the former scenario to be more consistent with data. Other papers, including this one, find self consistency without luminosity evolution.

We introduce here a new method for determining the rate and luminosity, and analyze the observations directly, without having any a-priori assumptions on the functional form of the luminosity and rate functions. This direct inversion allows us to use most of the available redshift data.

In §2 we describe the sub-sample of bursts we analyze and its advantages over other samples. In §3 we introduce a new formalism allowing us to directly extract the luminosity and rate functions. In §4 we present the results obtained using this method, and the confidence ranges associated with them. In §5 we test whether the GRB rate that we obtain is consistent with the SFR. We also examine models in which the GRB rate is frozen following different SFR models. We discuss a few implications of the results in §6.

2 THE SAMPLE

Our sample includes long bursts ($t_{90} \geqslant 2sec$) with a measured peak-flux, and with a measured redshift detected by the *Swift* satellite from the beginning of its operation until burst 090726 [1]. GRBs redshifts are acquired from the spectrum of the optical afterglow using absorption lines or photometry, or using emission lines detected in the spectrum of the host galaxy. We find different redshift distributions for the different detection methods, namely: Absorption lines, Emission lines, and Photometry (see Figure 1). We observe that using the host's emission lines, we do not detect high-redshift events, whereas absorption lines extend over the entire range of redshifts. Furthermore, the emission lines are more susceptible to a selection effect known as the 'redshift desert' in the range $1.1 < z < 2.1$ [2], (Fiore et al. 2007, see also Coward 2008). This later method - i.e. spectroscopy of the afterglow - become the dominant one for *Swift* bursts. It became possible with *Swift*'s quick alert for GRB position and replaced the emission line method that was used during the BeppoSAX era. We have also found that the probability to measure the redshift using emission lines strongly depends on the gamma ray flux, favoring high fluxes [3]. This effect is mild for absorption lines and photometry (see appendix B).

To obtain a more uniform sample we keep only bursts whose redshift was measured using the afterglow. For each burst we calculate the isotropic equivalent peak-luminosity: L_{iso} (see Appendix A. for details) using the peak-flux and redshift. We use standard ΛCDM cosmology with $h = 0.7, \Omega_m = 0.27, \Omega_\Lambda = 0.73$.

[1] All data were taken from the *Swift* information page $http://swift.gsfc.nasa.gov/docs/swift/archive/grb\_table/$

[2] Although redshift determination through absorption lines is also difficult in the range $1.5 < z < 2.1$

[3] A possible explanation is that brighter burst can be more easily localized, hence a follow-up be possible.

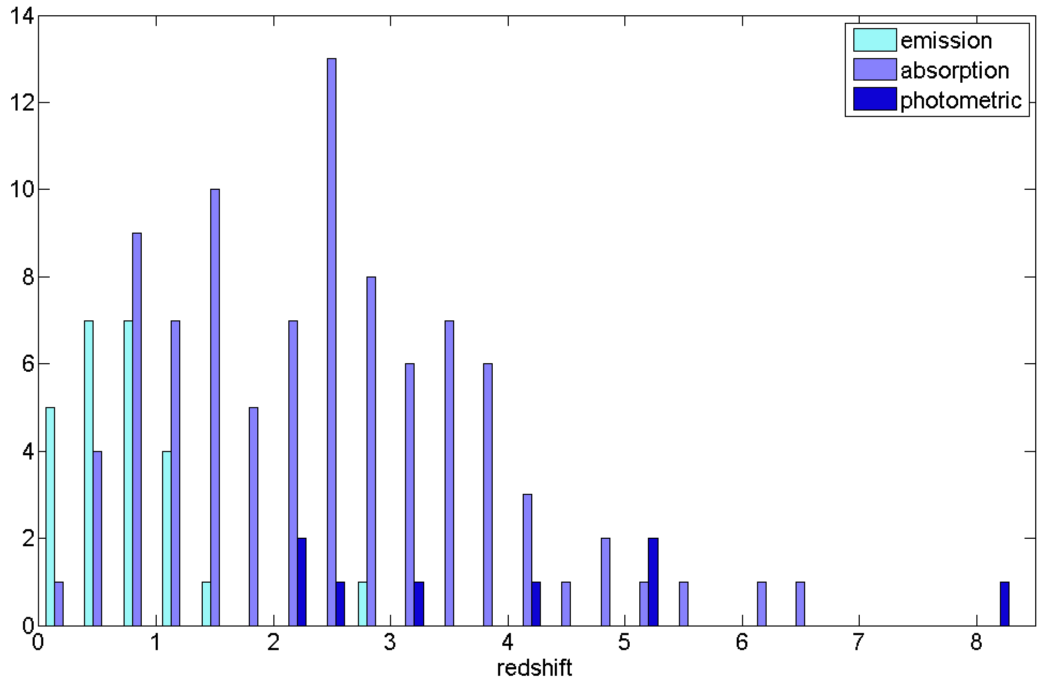

Figure 1. Redshift distribution for the different obtaining methods

This figure shows an histogram of the bursts redshifts, separated into 3 groups: by Absorption lines, by Emission lines, and Photometrically.

3 A DIRECT ESTIMATE OF THE LUMINOSITY FUNCTION AND THE RATE

Previous methods used the peak flux distribution and assumed a GRB rate and estimated the corresponding luminosity function. With the availability of a sample of GRBs with measured redshifts we present here a direct method to estimate both the luminosity and the rate.

3.1 Assumptions

We assume that the number of bursts at a given redshift and with a given luminosity is the product of two independent functions: The luminosity function, $\phi(L)$, that depends only on the luminosity L, and the GRB rate, $R_{GRB}(z)$, that depends only on the redshift z. This common assumption is reasonable since a-priori there is no competing reason why the luminosity function should depend on the redshift. The validity of this assumption is later tested and found to be accepted with a high statistical significance.

The isotropic peak luminosity function, $\phi(L)$, is defined traditionally as the fraction of GRBs with isotropic equivalent luminosities in the interval log L and logL + dlogL. The rate $R_{GRB}(z)$ is the co-moving space density of GRBs in the interval z to $z + dz$. We look for the functions that will give the distribution density:

$$n(L,z)dlogLdz = \phi(L) \cdot R(z)dlogLdz \ , \tag{1}$$

where

$$R(z) = \frac{R_{GRB}(z)}{(1+z)} \frac{dV(z)}{dz} \ , \tag{2}$$

is the differential co-moving rate of bursts at a redshift z, $dV(z)/dz$ is the volume element , and the factor $(1+z)^{-1}$ is due to the cosmological time dilation.

3.2 Formalism

We consider now a direct method to invert the observed $\{L_i, z_j\}$ distribution and obtain the functions ϕ and R_{GRB}. The advantage in this method, is that we determine both the rate and the luminosity function. Furthermore we don't assume a specific functional form for either functions. To do so we approximate $\phi(L)$, and $R(z)$ as $step functions$. A $step function$ is a function whose range divided to bins, having a constant value within each bin. It can be expressed as a sum of Heaviside functions.

First, we divide both luminosity and redshift intervals into bins. We denote

$$\phi_i \equiv \phi(L_i < L < L_{i+1}) \ , \tag{3}$$

$$R_j \equiv R(z_j < z < z_{j+1}) = \frac{1}{(z_{j+1} - z_j)} \int_{z_j}^{z_{j+1}} dz \frac{R_{GRB}(z_j)}{(1+z)} \frac{dV(z)}{dz} \ . \tag{4}$$

We also define the *weights factor*

$$w_{ij} \equiv \int_{L_i}^{L_{i+1}} \int_{z_j}^{z_{j+1}} \theta(L,z) dlogLdz \ , \tag{5}$$

as the *probability for detecting a burst with a measured redshift z and luminosity L* where $\theta(L,z) \equiv \theta_z(p(L,z))$ is the probability to detect and measure redshift for a burst with luminosity L at redshift z (see appendix B).

We denote the observed number of events per bin as:

$$N_i \equiv N(L_i \leqslant L < L_{i+1}) \ , \tag{6}$$

$$N_{,j} \equiv N(z_j \leqslant z < z_{j+1}) \ , \tag{7}$$

$$N_{ij} \equiv N(L_i \leqslant L < L_{i+1}, z_j \leqslant z < z_{j+1}) \ , \tag{8}$$

$$N \equiv \sum_{ij} N_{ij} \ . \tag{9}$$

Next, we determine ϕ_i and R_j, and the error estimates, using the maximum-likelihood formalism. We define M the (logarithmic) likelihood of the observations given the data as:

$$M = \sum_{ij} N_{ij} ln[\phi_i R_j w_{ij}] - N ln[\sum_{ij} \phi_i R_j w_{ij}] \ . \tag{10}$$

At the maximum all partial derivatives of M with respect to ϕ_i and with respect to R_j vanish, leading to

$$\phi_i = \frac{N_i}{\sum_j R_j w_{ij}} \frac{\sum_{i'j'} \phi_{i'} R_{j'} w_{i'j'}}{N} , \tag{11}$$

and

$$R_j = \frac{N_{,j}}{\sum_i \phi_i w_{ij}} \frac{\sum_{i'j'} \phi_{i'} R_{j'} w_{i'j'}}{N} . \tag{12}$$

Notice that the second term on the right hand side of each of the equations is just a normalization factor. We have a set of non-linear equations with as many equations as variables. Thus a-priori it is not clear whether ϕ and R are uniquely determined, and whether there is a solution at all. We solve these equations iteratively using various initial guesses. We find a convergence to a unique solution.

3.3 Error Estimates

We approximate the error as the value making M deviate by -1 from it's maximum: (i.e. the likelihood is a factor e smaller, this reflects a 1σ error for a normal-distribution)

$$-1 = N_i ln(1 + \frac{\Delta\phi_i}{\phi_i}) - N ln(1 + \frac{N_i}{N}\frac{\Delta\phi_i}{\phi_i}) , \tag{13}$$

$$-1 = N_{,j} ln(1 + \frac{\Delta R_j}{R_j}) - N ln(1 + \frac{N_{,j}}{N}\frac{\Delta R_j}{R_j}) . \tag{14}$$

The two solutions of $\Delta\phi_i/\phi_i$ or $\Delta R_j/R_j$, i.e. the positive one and the negative one, give an upper and a lower bounds on the error respectively. For small deviations, we can approximate the error using the second derivatives of M:

$$\frac{\Delta\phi_i}{\phi_i} \simeq \frac{\sqrt{2}}{\sqrt{N_i(1 - N_i/N)}} , \tag{15}$$

$$\frac{\Delta R_j}{R_j} \simeq \frac{\sqrt{2}}{\sqrt{N_{,j}(1 - N_{,j}/N)}} . \tag{16}$$

4 RESULTS

The luminosity function and the rate that best fit the observations, using the method described above, are shown in Figures 2, 3. We also calculated the local events rate ρ_0. So far, we have not assumed any functional form for the luminosity function or for the rate. After we obtained the results in the form of step functions we can further model the results with any desired functional form (we will use power laws in this paper). In this manner, the quality of the fit can be measured using χ^2 statistics, and we can present the results more easily. We discuss the details of the fit

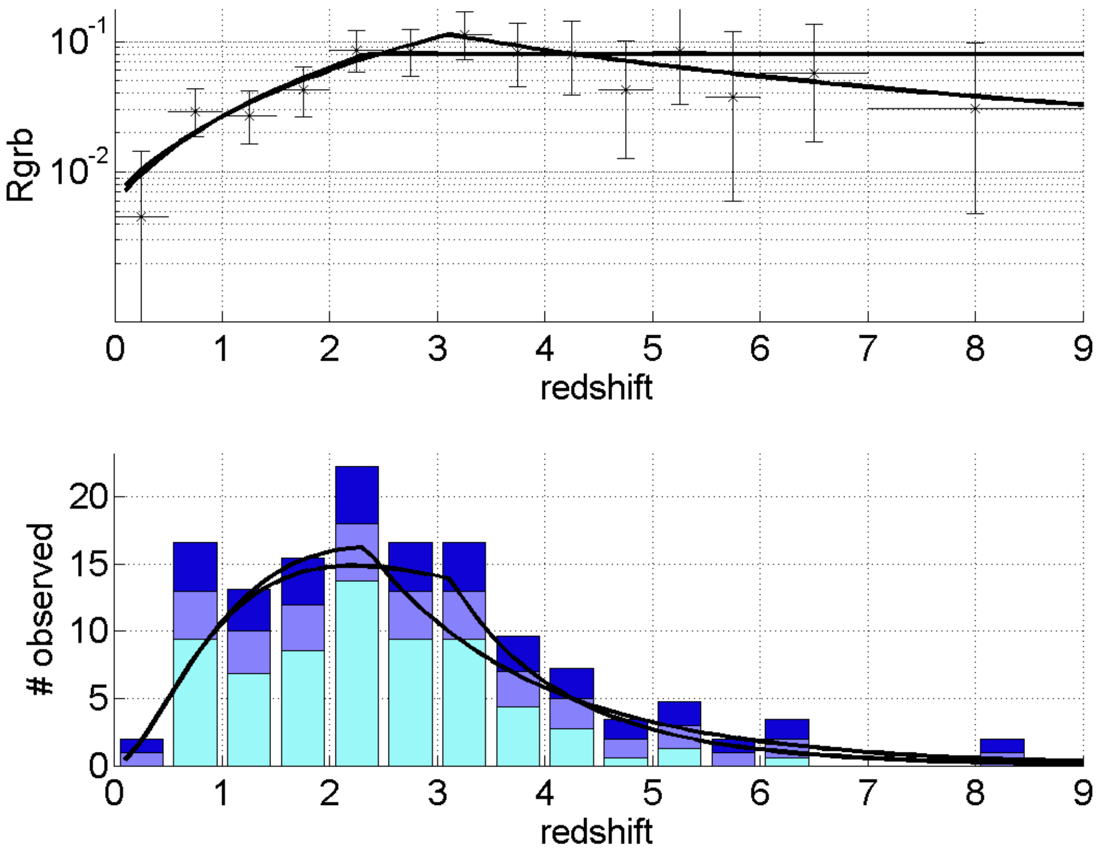

Figure 2. The comoving rate and the observed events number redshift distributions

Upper frame: The fits found for the rate: 1. a power law with index $n = 2.2$ in the range $0 < z < 2.4$, and a constant rate for $2.4 \leqslant z$. 2. a broken power law with indices $n_1 = 2.1$, $n_2 = -1.2$, and with a brake at $z = 3.1$. χ^2 for these models are 3.6 at 11 degrees of freedom, 2.3 at 10 degrees of freedom, this gives a rejection probability of 0.02, 0.007, for models 1, 2, respectively.
Lower frame: The number of detected bursts for each redshift bin, and the rates expected from the models fitted above. The two upper boxes in each column, represents the error range.

later on. The resulted are summarized in Tables 1, 2 where we present the parameters of a fit to a broken power law for the luminosity, and for two fits of broken power laws for the rate: one in which the second power law index is fixed to 0 (1 PL model), and a second one in which it is free (2 PL model).

To estimate the uncertainty induced by the specific bins choice, we preform all the analysis for a 1/2 unit binning, i.e. redshift bins are: $0 < z \leqslant \frac{1}{2}$; $\frac{1}{2} < z \leqslant 1$; ... $5\frac{1}{2} < z \leqslant 6$; $6 < z \leqslant 7$; $7 < z \leqslant 9$, and luminosity bins are $50 < logL \leqslant 50\frac{1}{2}$; $50\frac{1}{2} < logL \leqslant 51$; $...53\frac{1}{2} < logL \leqslant 54$, and repeat the analysis for a 1/3 unit binning (where all bins width are 1/3 unit, except the last two redshift bins which we cannot change because they contain too few data points). The error ranges quoted here are for the 2 PL model with the 1/2 unit binning, because this one gives the best results in the K-S tests (see §4.1). Hereafter unless otherwise stated we use this model for all

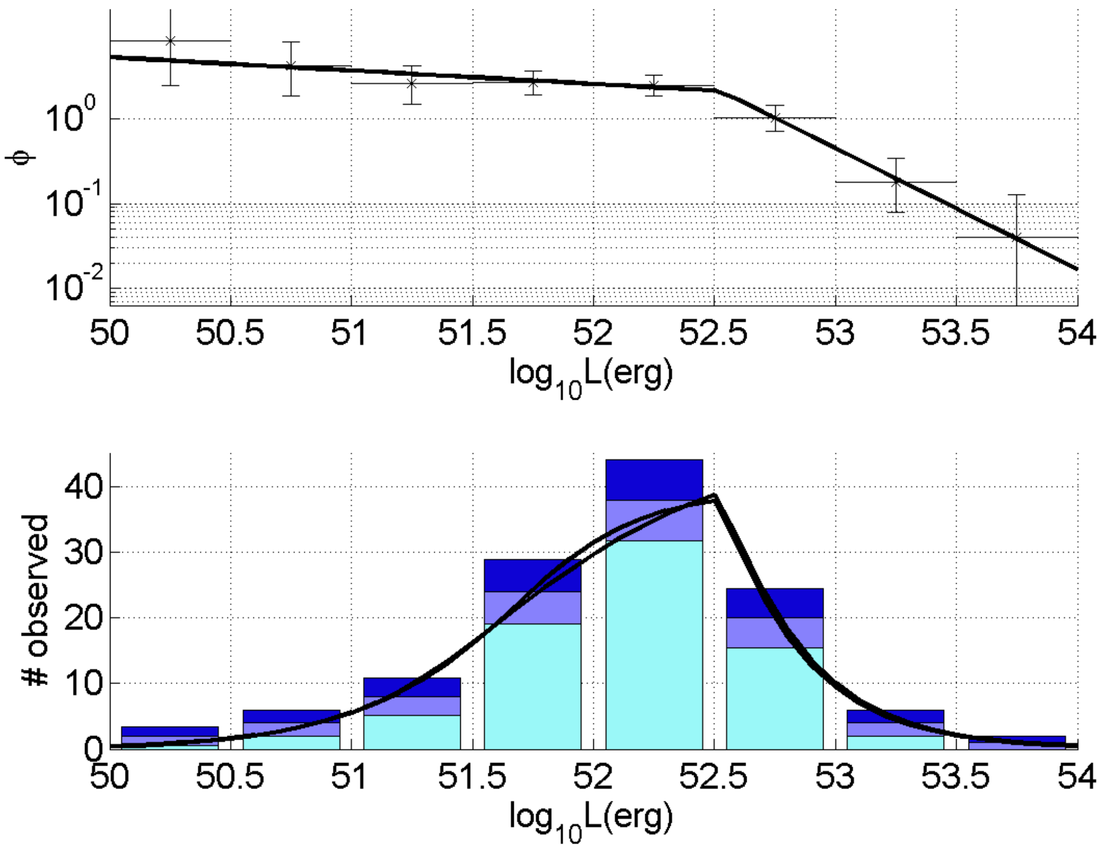

Figure 3. The luminosity function model fit and the observed and predicted luminosity distributions

Upper frame: The fit found for the luminosity function: a broken power law, with a break at $L* = 10^{52.5}$, a low luminosity index $\alpha = 0.2$, and a high luminosity index $\beta = 1.4$. χ^2 for this model is 0.63 at 4 degrees of freedom, this gives a rejection probability of 0.04.
Lower frame: The number of detected bursts for each luminosity bin, and the rates expected from the models fitted above. The two upper boxes in each column, represents the error range. The two lines coresponds to the two rate models considered (see previous figure).

	our result	sim median	$68\%min$	$68\%max$	$95\%min$	$95\%max$
$1/2bins$:						
$logL*$	52.53	52.54	52.30	52.69	51.98	53.19
α	0.17	0.14	-0.01	0.28	-0.20	0.39
β	1.44	1.49	1.11	2.01	0.86	8.54
z_1	2.35	2.25	1.82	2.80	1.38	4.25
n_1	2.22	2.12	1.56	3.02	1.10	4.44
ρ_0	1.13	1.22	0.58	1.98	0.22	2.95
$1/3bins$:						
$logL*$	52.58	52.59	52.37	52.72	51.92	52.83
α	0.18	0.15	-0.00	0.27	-0.18	0.38
β	1.59	1.63	1.24	2.17	0.93	3.58
z_1	2.60	2.50	1.90	3.50	1.42	8.46
n_1	1.86	1.88	1.24	2.62	0.81	3.99
ρ_0	1.56	1.55	0.84	2.54	0.27	3.91

Table 1. Function's parameters: PL and a flat

The first half of the table is for $1/2$ unit binning, the second half of the table is for $1/3$ unit binning. Both are results of Monte-Carlo simulations with 10000 sets, each of 101 data points. See footnote in §4 for the proper interpretation of the error ranges.

	our result	sim median	$68\%min$	$68\%max$	$95\%min$	$95\%max$
$1/2bins$:						
$logL*$	52.53	52.54	52.29	52.70	51.99	53.19
α	0.17	0.14	-0.02	0.27	-0.20	0.38
β	1.44	1.48	1.11	2.08	0.85	8.52
z_1	3.11	3.13	2.48	3.93	1.76	4.77
n_1	2.07	2.03	1.56	2.70	1.18	3.62
n_2	-1.36	-1.81	-3.75	-0.36	-8.19	0.05
ρ_0	1.25	1.26	0.69	1.95	0.32	2.77
$1/3bins$:						
$logL*$	52.58	52.58	52.37	52.72	51.90	52.83
α	0.18	0.15	-0.00	0.27	-0.19	0.38
β	1.59	1.61	1.23	2.17	0.93	9.45
z_1	3.45	3.45	2.50	4.28	1.78	6.09
n_1	1.74	1.82	1.33	2.39	0.91	3.35
n_2	-1.47	-1.92	-4.45	-0.17	-44.77	0.19
ρ_0	1.71	1.57	0.95	2.45	0.44	3.64

Table 2. Function's parameters: two PL

The first half of the table is for $1/2$ unit binning, the second half of the table is for $1/3$ unit binning. Both are results of Monte-Carlo simulations with 10000 sets, each of 101 data points. See footnote in §4 for the proper interpretation of the error ranges.

further analysis. Clearly the best fit parameters of the other binning and of the other power laws model are slightly different, but they are all within each other's error range. All give good results in the KS-tests, almost as well as the best model. When we consider the uncertainty induced from the binning choosing, the error ranges become only slightly wider.

We fit the functions to power-laws, by minimizing the chi-square, for functions of the form:

$$\phi(L) = \begin{cases} (\frac{L}{L*})^{-\alpha} & L < L* \, , \\ (\frac{L}{L*})^{-\beta} & L > L* \, . \end{cases} \tag{17}$$

$$R_{GRB} = R_{GRB}(0) \cdot \begin{cases} (1+z)^{n_1} & z \leqslant z_1 \, , \\ C_1(1+z)^{n_2} & z > z_1 \, , \end{cases} \tag{18}$$

$$C_1 = (1+z_1)^{n_1 - n_2} \, .$$

The luminosity function is well described by a broken power law, with a break at $L* \simeq 10^{52.5\pm0.2}[erg/sec]$ and with indices $\alpha = 0.2^{+0.2}_{-0.1}$ and $\beta = 1.4^{+0.3}_{-0.6}$. The fit for a broken power law, is very good, giving $\chi^2 = 0.64$ for 6 degrees of freedom. This result agrees with previous studies (e.g. Daigne et al. 2006; Guetta and Piran 2007). The luminosity function cannot be fitted with a single power law, since such fit give high χ^2 results thus rejecting such a model with high significance (98%). The rate is described as well by a broken power law for $1 + z$, with a break at $z = 3.1^{+0.6}_{-0.8}$, and indices of $n_1 = 2.1^{+0.5}_{-0.6}$, and $n_2 = -1.4^{+2.4}_{-1.0}$. This GRB event rate is different from the SFR: While the SFR shows a steeper rise from $z = 0$ to $z = 1 - 1.5$, this rate rises less steeply and continues rising till $z \simeq 3$. The overall rise is by a factor of $10 - 20$, which is comparable to the rise in the SFR. The decline above $z \simeq 3$, is shallow, and dose not agree with the SFR as in Hopkins and

Beacom (2006), (see Figure 9). However the SFR at high redshift is uncertain and there are models that suggest that the SFR dose not decline at high redshifts, like SF2 in Porciani and Madau (2001) or Rowan-Robinson (1999) and SF3 of Porciani and Madau (2001) even rises. The local events rate we find is $\rho_0 \simeq 1.3^{+0.6}_{-0.7}[Gpc^{-3}yr^{-1}]$, in agreement with previous studies, e.g. Schmidt (1999)($\rho_0 \simeq 1.5$), see however Schmidt (2001b)($\rho_0 \simeq 0.15$)); Guetta et al. (2005)($\rho_0 \simeq 0.5$).

In order to examine the dependence of result on the specific binning chosen, we repeat the calculations for different binning of the data. In all cases we preformed a Monte-Carlo simulation to estimate the error ranges for each of the parameters in the models, and for the local events rate. The results are shown in Tables 1, 2.

In the Monte-Carlo simulation we use the model with the best fit parameters, to draw a new random set of data - having the same size as the real data sample. We then carry on the analysis on this mock data set and obtain new best fit parameters (which deviate from the original ones). Repeating this process many times - starting again from the original best fit parameters - we obtain a scatter of points in the parameters plane, around the original best fit parameters. The central 68%, and 95% range of these points for each of the parameters separately, are shown in tables 1, 2. [4].

4.1 Consistency Checks

We have assumed that the luminosity function and the rate can be separated. We must check the validity of this assumption before we can accept the model. To do so, we preform a two dimensional equivalent of the Kolmogorov-Smirnov test (see Fasano and Franceschini (1987), Peacock (1983), Spergel et al. (1987)). In this test the two dimensional data is compared to the modeled distribution for each of 4 quadrant defined by axes crossing at each data point. The maximal difference is used to estimate the probability that the data is drawn from the distribution implied by the model. The number displayed in the table's 2D K-S column is the probability that the models fits the data. In our models, the test gives high probabilities (86%, 98% for models 1 PL , 2 PL respectively), so we can accept the model and justify the underling assumption (of luminosity function being redshift independent).

We carry out two other consistency checks: First, we compared the peak flux distribution expected by our model, to the observed ones, by BATSE, and by *Swift*. The results are shown

[4] When reading the error ranges from these tables we switch between the (+) and (-) error ranges i.e. A^{+x}_{-y} is replaced by A^{+y}_{-x}. This is done to approximate the range of parameters where it is probable (that by drawing a random sample from it) they have led to our best-fit parameters, rather than the range of parameters where it is probable to get to (by drawing a random sample) from our best-fit parameters - which is what the MC simulation gives.

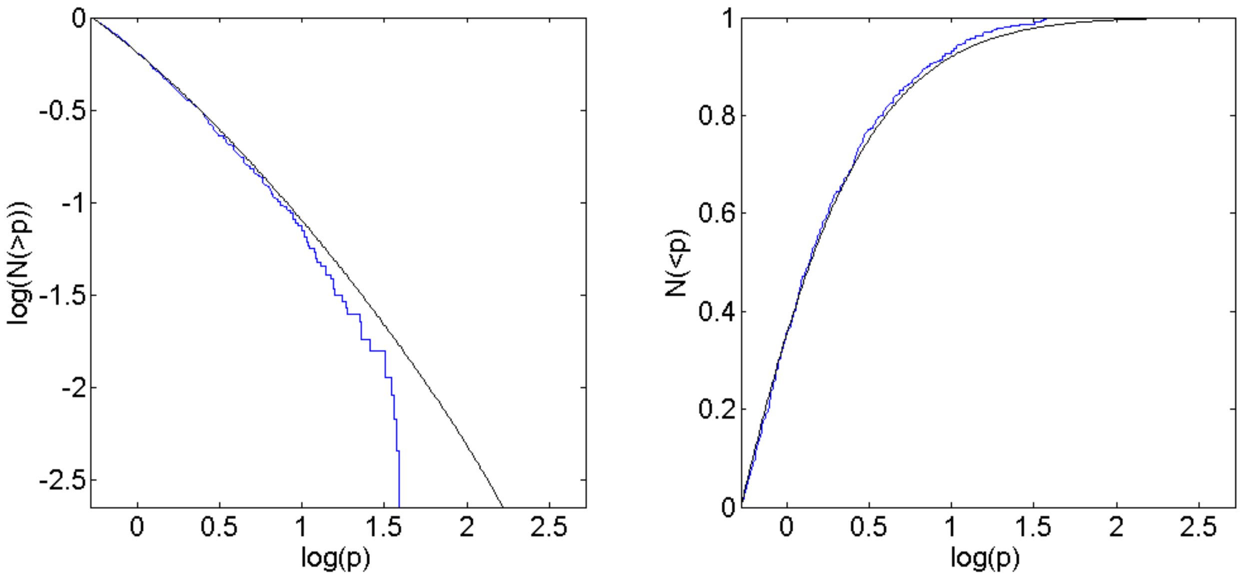

Figure 4. Bursts count vs. peak flux for BATSE bursts

Cumulative bursts distribution as a function of the peak flux p. Left: logarithmic scale. showing $N(<p)$ Right: log linear scale showing $N(>p)$, this is used for the KS-test, giving probability of 87%, thus acceptable.

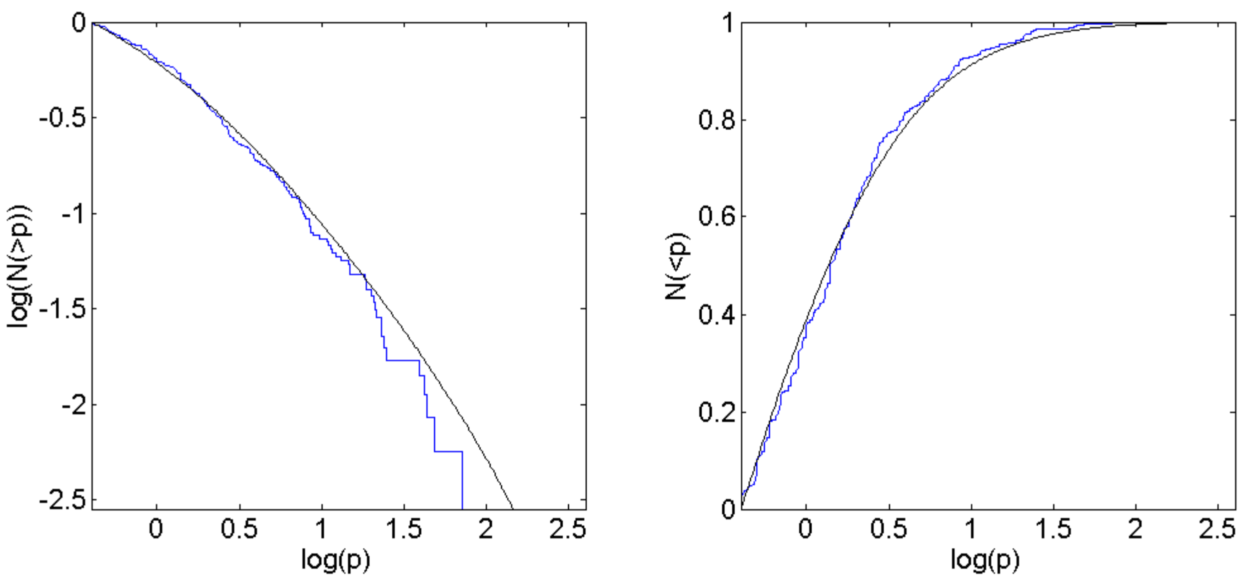

Figure 5. Bursts count vs. peak flux for *Swift bursts*

Cumulative bursts distribution as a function of the peak flux p. Left: logarithmic scale. showing $N(<p)$ Right: log linear scale showing $N(>p)$, this is used for the KS-test, giving probability of 17%, thus acceptable.

in figures 4, and 5. The KS-test results: 87% for BATSE bursts and 17% for *Swift* bursts, (a model is rejected when the KS-test result is less than 5%). We note here, that the model is significantly rejected (KS-test $< 10^{-5}$) when compared to BATSE peak fluxes distribution for flux $> Plim = 0.25 ph/cm^2/sec$. However, when applying the effective detection threshold calculated by Band (2002) of $Plim = 0.525 ph/cm^2/sec$, the model is accepted with high significance (87%).

Second, we compared the cumulative redshift distribution, to the observed one, and preformed a KS-test. Here as well, the test results give high probabilities (59%, 57% for models 1 PL , 2 PL respectively), for accepting the model.

4.2 A Comparison With the Complete *Swift* Sample

Our results are based only on the absorption and photometric determined redshifts of the *Swift* sample. Recently, Fynbo et al. (2009) obtained emission lines redshift measurements for GRBs host galaxies that were not measured before. Most of those are at low redshifts. The growing number of emission lines redshifts in the range $0 < z < 1$ raises the question whether our model - based on a sample of redshifts measured from the afterglows - is consistent. We used our model to calculate the expected redshift distribution of the entire bursts population and compared it to the number of observed bursts with a known redshift (measuered using all methods). Clearly for any range of redshifts the number of bursts with known redshift should not exceed the number predicted by our model for the entire bursts population. Fig 6 depicts this comparasion for the cumulative number and for the counts number in redshift bins. Our model is consistent for all redshifts $\gtrsim 0.4$. However there is an excess of low redshift bursts not predicted by our model. The main cause of the discrepancy are three bursts with $z < 0.1$ where according to the model no such bursts are predicted. Without these three bursts the model pass this consistency check. Note that these three bursts at low redshifts where detected with emission lines and but no burst was detected in this range using absorption lines. These three bursts rate is significantly higher than predicted by the model and cannot be explained by misidentification of galaxies with bursts afterglows as this effect is too small (Cobb and Bailyn (2008)). Also note that even though they are at low redshifts these three bursts all have low luminosities, and they possibly represent a low luminosity bursts population which is different from the majority of the bursts (see discussion in §6.2).

4.3 The Redshift Distribution and Expectations for Future Missions

We present the observed cumulative redshift distribution, and the predicted one, for high redshifts bursts for *Swift* and for past and future missions: BATSE, EXIST (Band et al. 2008) and SVOM (Schanne 2008; Gotz et al. 2009) in figure 7. A particularly interesting question is how many high redshift bursts are expected to be observed, because such bursts may shed new light on the very early universe. Already now GRB090423 is the most distant and hence the earliest object observed

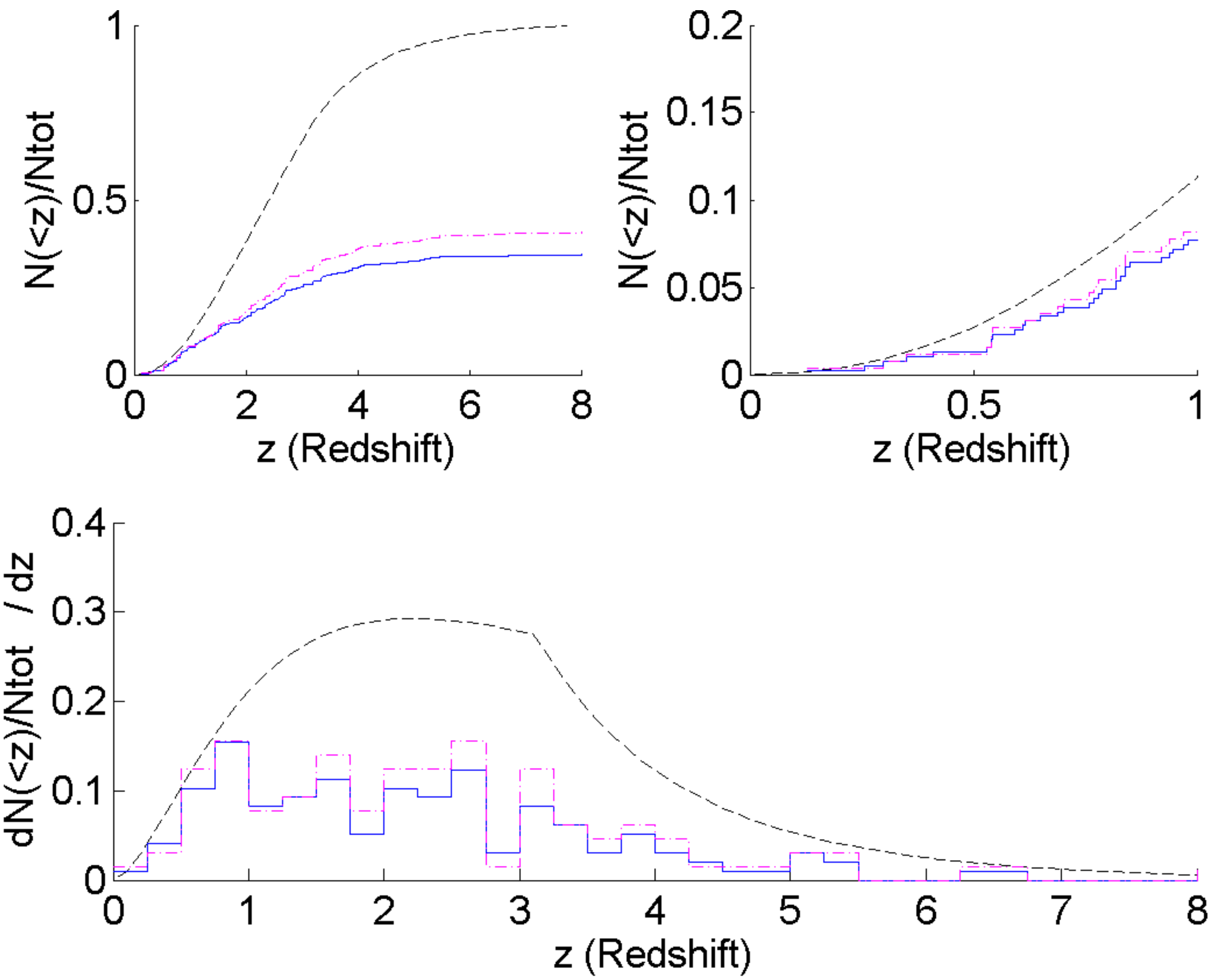

Figure 6. Redshift obtained by any method compared to the total number of bursts predicted by the model

Upper frames: Left: The cumulative total fraction of bursts predicted by the model (dashed curve) and the detected cumulative fraction of bursts with redshift obtained by any method (solid steps), as a function of the redshift. Right: Zoom in on the low redshift part of the left figure. Lower frame: The number density (per unit redshift) of bursts predicted by the model (dashed curve) and an histogram of bursts with redshift obtained by any method (solid steps), both normalized by the total number of bursts. For all frames: The number of bursts with redshifts taken form and normalized out of the bursts which had an at slew, i.e. the time elapsed form the trigger until the first optical observation < 300 sec (dashed dotted steps).

so far. We calculate the fraction of bursts with $z > 7, 8, 9, 10, 15, 20$ respectively. The results are presented in table 3.

Detection of high redshift bursts is one of the main objectives of EXIST. The number of high redshift bursts expected to be detected by EXIST is presented in table 4. for the different models and parameters. During a five year mission EXIST will detect many high redshift ($z > 10$) bursts for the 1 PL model ($\approx$ 99 bursts), even more for the 2 PL model with the highest high-redshifts index $n_2 = 1.03$ in the 68% error range ($\approx$ 350 bursts), much fewer when taking the best fit parameters $n_2 = -1.36$ ($\approx$ 28 bursts), and less for the lowest high-redshifts index $n_2 = -2.36$ in the 68% error range ($\approx$ 10 bursts) - but still higher than expected for *Swift*. In the best-fit model

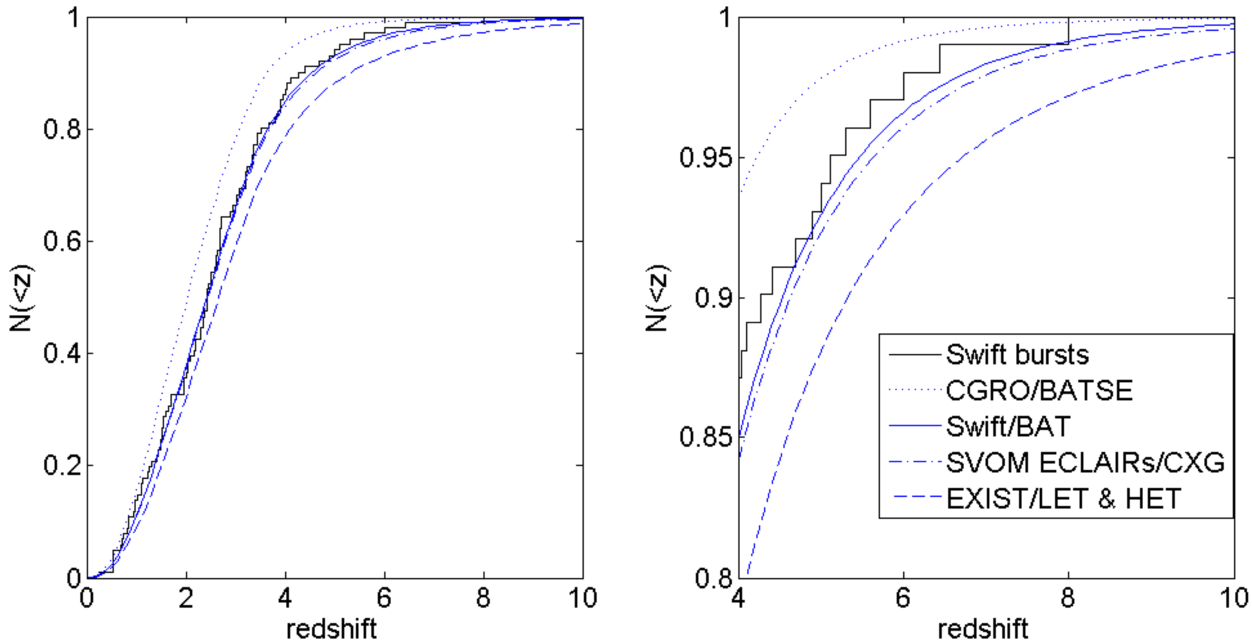

Figure 7. Cumulative redshift distribution for *Swift* bursts

Cumulative redshift distribution of *Swift* observed bursts, and the model prediction (solid line). KS-test, giving probability of 57% ,thus acceptable. Also presented the prediction for some past and future missions: BATSE, SVOM, and EXIST. Right frame is a zoom-in to the upper right part of the left frame.

fraction of $z >$	7	8	9	10	15	20
CGRO/BATSE	0.4%	0.2%	0.1%	0.05%	0.01%	0.002%
Swift/BAT	1.7%	0.9%	0.5%	0.3%	0.03%	0.01%
SVOM ECLAIRs/CXG	2%	1.2%	0.7%	0.4%	0.06%	0.02%
EXIST/LET & HET	4%	3%	2%	1%	0.2%	0.06%

Table 3. High redshift fraction prediction for *Swift* and several other missions.

there is a good probability to see a $z > 20$ burst, as it predicts ≈ 1 bursts in EXIST's five year mission.

EXIST's bursts per year for $z >$	7	8	9	10	15	20
2 PL $n_2 = 1.03$	144	110	90	70	26	12
1 PL $n_2 = 0$	54	38	27	20	5	1.6
2 PL $n_2 = -1.36$	23	14	9	6	0.9	0.2
2 PL $n_2 = -2.36$	11	6	3	2	0.2	0.04
SVOM's bursts per year for $z >$	7	8	9	10	15	20
2 PL $n_2 = 1.03$	14	10	7	5	2	0.8
1 PL $n_2 = 0$	5	3	2	1.5	0.3	0.1
2 PL $n_2 = -1.36$	2	1	0.7	0.4	0.06	0.01
2 PL $n_2 = -2.36$	1	0.5	0.2	0.1	0.01	0.003

Table 4. High redshift detection rate prediction for EXIST and for SVOM. On average redshift is obtained for only a third of the events.

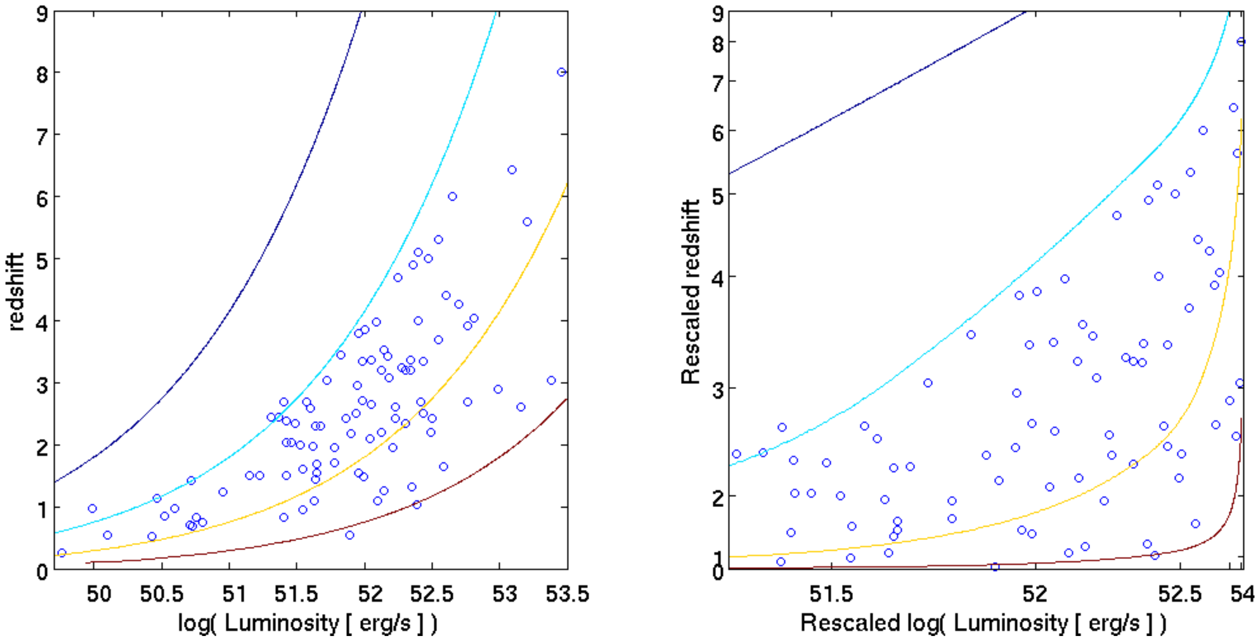

Figure 8. Redshift Bursts on the L-z plane

The bursts distribution in the Luminosity-Redshift plane. Left: linear scale. Right: Axes are rescaled using $R(z)$ and $\phi(L)$, so that we have a uniform bursts-number density. The curved lines are contour lines for equal fluxes, for the values: $p = 0.04, 0.4, 4, 40[ph/sec/cm^2]$, from top to bottom. The $p = 0.4[ph/sec/cm^2]$ line is our detection threshold. The number density is uniform in the rescaled plane as expected, and it drops to zero below the detection threshold.

4.4 The Rescaled L-z Plane

To illustrate the distribution of bursts, we now display the bursts in the $L - z$ $(Luminosity - Redshift)$ plane and in a rescaled plane in which the number of detected bursts (with or without redshift measurement) is proportional to the area (Fig. 8).

5 THE GRB RATE AND SFR

We recall that for a long time it was assumed that the GRB rate follows the SFR. We turn now to test this hypothesis. The same tests used in §4.1, can be used now to check the consistency of the data with a rate proportional to the star formation rate (SFR). An obvious problem is that SFR is not uniquely determined and hence we must consider four different possible SFRs that have been suggested: Hopkins and Beacom (2006) (denoted HB), SF2 of Porciani and Madau (2001) (denoted PM SF2), Rowan-Robinson (1999) (denoted R-R) and SF3 of PM (denoted PM SF3). Note that the first function decreases at large redshift, which the second and third are constant and the forth one increases at a large redshift. We compare, first, the SFRs to the binned rate we obtained by inverting the data (see Figure 9), and we calculate the χ^2 for both $1/3$ and $1/2$ binning. We find acceptable reduced χ^2 values (see Table 5) for all four functions. However, a comparison of the overall observed redshift and luminosity distributions with those predicted by models in

	reduced χ^2 (1/3 bins)	reduced χ^2 (1/2 bins)	2D K-S	peak flux K-S test	z K-S test	$L*$	α	β
1 PL & flat	0.30	0.33	0.86	0.83	0.59	52.53	0.17	1.44
2 PL	0.24	0.23	0.96	0.82	0.62	52.53	0.17	1.44
HB	1.17	1.44	$2 \cdot 10^{-5}$	$5 \cdot 10^{-5}$	$9 \cdot 10^{-8}$	52.53	0.17	1.44
HB	1.17	1.44	0.002	$4 \cdot 10^{-9}$	$7 \cdot 10^{-5}$	52.49	-0.13	1.46
PM SF2	0.55	0.60	0.06	0.03	0.01	52.53	0.17	1.44
PM SF2	0.55	0.60	0.16	0.01	0.08	52.48	-0.00	1.48
R-R	0.70	0.86	0.004	$7 \cdot 10^{-4}$	$2 \cdot 10^{-4}$	52.53	0.17	1.44
R-R	0.70	0.86	0.06	$2 \cdot 10^{-5}$	0.01	52.46	-0.07	1.48
PM SF3	0.49	0.56	0.46	0.49	0.11	52.53	0.17	1.44
PM SF3	0.49	0.56	0.68	0.78	0.18	52.46	0.10	1.50

Table 5. Statistical tests for our models and for models following one of the SFRs models considered.

which the GRB rate if fitted by an SFR reveals that the 2D K-S or the K-S tests for the peak flux distribution and for the redshift distribution show inconsistency for the first three functions. We find consistency for the forth one, which is the only one that increases at large redshift.

Adding further freedom to the model by optimizing the luminosity function for a given SFR. We take the GRB rate as known following a model of the SFR and obtain the best fit luminosity function for each model by solving equation 11. We now perform a 2D K-S test to these functions, and we also perform K-S tests for the peak flux distribution and for the redshift distribution. The results of the statistical tests are shown in Table 5. Even though the fit improves still the first three SFR models fail the KS tests and only the forth one, SF3 of PM, with a rising SFR at high redshifts is consistent with acceptable K-S tests.

We attribute the consistency of the GRB rate with the SF3 but not the other SFR to the fact that like our model but unlike other SFRs, it shows a rising rate the range $1 < z < 3$. Unlike our model SF3 model continues to increase also for $3 < z$, but that paucity of data points at this range leads to large error bar so that SF3 is consistent with observations. This result agrees with Daigne et al. (2006) that examined Porciani and Madau (2001) SFRs and concluded that GRB rate which follows SF3 is the only consistent model and with Guetta and Piran (2007) that suggest that at high redshifts the GRB rate is higher. We stress however, that more recent work (e.g. Mannucci et al. 2007) on the SFR suggest that it does decreases at high redshifts and thus, it is not clear that SF3 is a viable SFR model in view of the recent data.

6 SUMMARY AND CONCLUSIONS

6.1 GRBs Rate and the SFR

For a luminosity function that is redshift independent, we can rule-out the hypothesis that the GRB rate follows the SFR for all SFR models which are not rising at high redshifts. A SFR

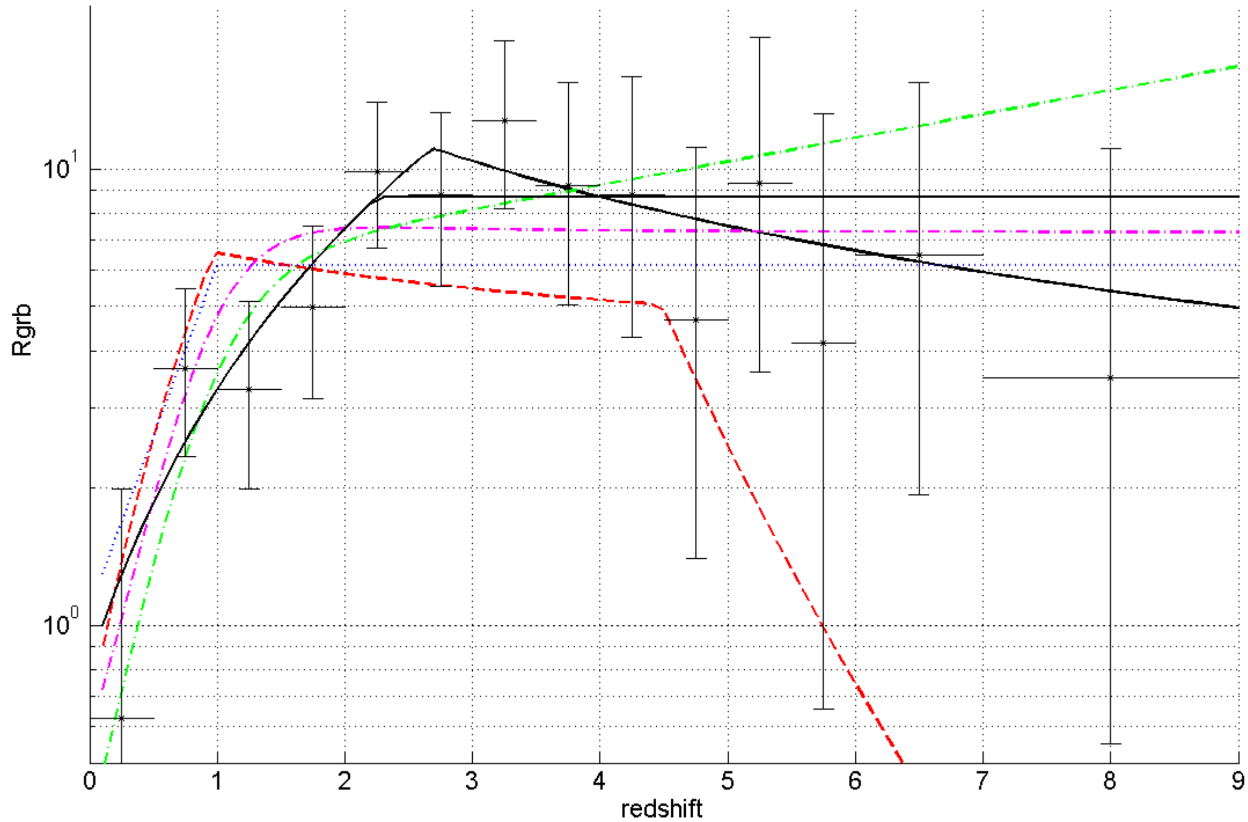

Figure 9. GRB events rate, and several star formation rates

The results for the rate, in 1/2 unit binning. Best fit for two power laws, and for a power law and a flat (the second index fixed to 0) - solid line. Hopkins and Beacom (2006) SFR - dashed line. SF2 and SF3 of Porciani and Madau (2001) - dashed dotted line. Rowan-Robinson (1999) SFR - dotted line. All normalized to the same value at $z = 0$.

that rises at high redshifts, like SF3 of PM is acceptable but such model is not favored by most recent SFR observations, see discussion in §5). This conclusion holds for various SFR models. The main difference of our model from the SFR is that the GRBs rate rises in the range $0 < z \lesssim 3$, while the SFR rises much more steeply with about the same factor of $10 - 20$, within the range $0 < z \lesssim 1$. The low redshift parts of both the SFR and the GRB rate are more tightly constrained. The SFR rate in this range is almost the same for the different SFRs considered (Rowan-Robinson 1999; Porciani and Madau 2001; Hopkins and Beacom 2006). The high redshift part of the SFR is less constrained, and it differs from one SFR model to another. However the low redshift part is sufficient to reject all SFR models, regardless of their high redshift part. The only exception, SF3 of PM is consistent with the GRB rate because it continues to rise (albeit at a slower pace) at the range $1 < z < 3$. This conclusion is consistent with a number of recent works, all concluding that the GRB rate can't simply follow the SFR (e.g. Guetta and Piran 2007).

The model we find for the GRB rate, shows an increase in rate up to redshift $\simeq 3$, and is compatible with a constant rate at higher redshifts. However we obtain a slightly better fit with a shallow decline at $z > 3$ ($n_2 \simeq -1.4$), with 68% confidence limits ranging from a steep decline

($n_2 \simeq -2.4$), to a positive incline ($n_2 \simeq 1$). The model is consistent with all statistical tests, and thus we can accept the basic assumption that the luminosity function dose not evolve with time.

The diversity of GRBs rate and the SFR, can be explained within the framework of the massive stellar collapse model. The relation to metalicity, (Woosley 1993) may suggest that GRBs rate follows the low-metalicity part of the star formation. However, Fynbo et al. (2009) recently found that the optical afterglow spectroscopy sample is biased against measuring redshift at high metalicity environments, meaning that the result might be an artifact of a selection effect. To check whether there are bursts populations not represented by our sample we preformed a consistency check described at §4.2 comparing our results with bursts with redshit obtained by any method. We find an overall consistency but also three low redshift and low luminosity bursts (with emission lines redshifts) that represent a significant population of weak bursts that are not observed at high redshifts and whose distribution is not a simple extrapolation of the rest of the bursts. (see §6.2 below).

6.2 Low Luminosity Bursts

The faintest burst in our sample GRB050724 has $L_1 = 10^{50.4}[erg/sec]$. By applying our best fit model, we expect 0.9 bursts with $L \leqslant L_1$, in the time span of our sample (4.5 years). *Swift*s weakest burst: GRB060218 (Cusumano et al. 2006) $L_2 = 10^{47.4}[erg/sec]$, is not in our sample because it has only emission lines redshift. Assuming that we can extrapolate the power-laws found, using our best-fit model we expect $2.5 \cdot 10^{-6}$ bursts with $L \leqslant L_2$. Even when applying the 95% level of the parameter $\alpha = 0.38$, we expect no more than $5 \cdot 10^{-5}$ bursts with $L \leqslant L_2$. This implies that this burst represent a population of fainter GRBs, with much higher events rate, which cannot be directly extrapolated to the stronger GRB population. This result is in agreement with other studies (e.g. Cobb et al. 2006; Liang et al. 2007). The emission lines redshifts sample includes two other low luminosity bursts are discovered: GRB051109 and GRB060505 with $z = 0.08, 0.089$, and $L = 10^{48.6}[erg/sec], 10^{49.4}[erg/sec]$. The detection probability of such bursts, according to our model is $< 2 \cdot 10^{-3}, 2 \cdot 10^{-2}$ respectively. These three low luminosity bursts must belong to a different and a distinct group and we remove them from the analysis when checking for consistancy in §4.2.

6.3 High Redshift Bursts

Higher redshift bursts are most interesting as they can provide clues on the very early universe. Extrapolating the rate for very high redshifts, we expect ~ 0.9 bursts with $z > 8$ and ~ 0.5 bursts with $z > 9$ (bursts with measured redshift), detected by *Swift* in the time span of our sample (4.5 years), which is consistent with the observations. Future missions like EXIST, can find many more such bursts, tens or even hundreds of $z > 10$ bursts (see §4.3).

6.4 The Local Event Rate

The local event rate found is $\rho_0 = 1.3^{+0.6}_{-0.7}[Gpc^{-3}yr^{-1}]$. Having one galaxy in $100Mpc^3$ this rate is equivalent to 1 event per galaxy per 10^7 years! Taking into consideration the beaming factor of about 50 (see Guetta et al. (2005)), the total events rate is about 1 event per galaxy per $2 \cdot 10^5$ years.

One implication of this result will be the association of gamma ray bursts with global extinctions of biologic spices on earth which occurred a factor of 10 times less frequent, about once every 100 Myr. These two rate may be matched if the events rate in the Galaxy is lower than the average local events rate, possibly because Galaxy forms stars at lower rate, or by posing further requirements for the burst to cause extinction: like a minimal flux, minimal hardness, or minimal fluence.

ACKNOWLEDGMENTS

We thank Shiho Kobayashi, Ehud Nakar and Elena Rossi for fruitfull discussions. The research was supported by an ERC Advanced Research Grant, by the ISF center for High Energy Astrophysics and by the Israel-France program in Astrophysics grant.

REFERENCES

Band, D.L., et al. 1993, ApJ, 413, 281.

Band, D.L., 2002, ApJ, 578, 806.

Band, D.L., 2006, ApJ, 644, 378.

Band, D.L., et al. 2008, ApJ, 673, 1232.

Barthelmy, S., et al. 2005, Space Sci Rev, 120, 143.

Berger, E., et al., 2005, ApJ, 634, 501.

Bromm, V., Loeb, A., 2006, ApJ, 642, 382.

Chary, R., Berger, E., Cowie, L., 2007, ApJ, 671, 272.

Cobb, B.E., et al., 2006, ApJ, 645, L113.

Cobb, B.E., Bailyn, C.D., 2008, ApJ, 677, 1157.

Cohen, E., Piran, T., 1995, ApJ, 444, L25.

Coward D.M., 2008, MNRAS, 393, L65

Cusumano, G., et al., 2006, GCN, 4775.

Daigne, F., Rossi, E. M., Mochkovitch, R., 2006, MNRAS, 372, 1034.

Fasano, G. and Franceschini, A. 1987, MNRAS, 225, 155.

Fenimore, E.E., et al., 1993, Nat, 366, 40.

Fiore, F., et al., 2007, A&A, 470, 515.

Firmani, C., et al., 2004, ApJ, 611, 1033.

Firmani, C., et al., 2005, Nuovo Cim, 28C, 665, arXiv:astro-ph/0504417.

Fynbo, J.P.U., et al., 2009, arXiv:0907.3449v1.

Galama, T.J., et al., 1998, Nature, 395, 670.

Gorosabel, J., et al. 2004, A&A, 427, 87.

Gotz, D., et al. 2009, AIP conf. proc., 1133, 25, arXiv:astro-ph/0906.4195v1.

Guetta, D., et al. 2005, ApJ, 619, 412.

Guetta, D., Piran, T., 2005, A&A, 435, 421.

Guetta, D., Piran, T., JCAP, 7, 3.

Hopkins, A.M., Beacom J.F., 2006, ApJ, 651, 142

Jakobsson, P., et al., 2006, A&A, 447, 897.

Kocevski, D., Liang, E., 2006, ApJ, 642, 371.

Le, T., Dermer, C.D., 2007, ApJ, 661, 394.

Le Floc'h, E., et al., 2006, ApJ, 642, 636.

Liang, E., et al., 2007, ApJ, 662, 1111.

Lloyd-Ronning, N.M., Fryer, C.L., Ramirez-Ruiz, E., 2002, ApJ, 574, 554.

Loredo, T.J., Wasserman, I.M., 1998, ApJ, 502, 75.

Mannucci, F., et al., 2007, A&A, 461, 423.

Mao, S., Paczynski, B., 1992, ApJ, 388, L45.

Matsubayashi, T., et al., 2006, Prog. Theor. Phys., 114, 983, arXiv:astro-ph/0509276.

Natarajan, P., et al., 2005, MNRAS, 364, L8.

Paczyński, B., 1998, ApJ, 494, L45.

Peacock, J.A. 1983, MNRAS, 202, 615.

Piran, T., 1992, ApJ, 389, L45.

Porciani, C., Madau, P., 2001, ApJ, 548, 522.

Preece, R.D., et al. 2000, ApJS, 126, 19.

Rowan-Robinson, M., 1999, Ap&SS, 266, 291.

Salvaterra, R., Chincarini, G., 2007, ApJ, 656, L49.

Salvaterra, R., et al. 2009, MNRAS, 396, 299.

Schanne, S., 2008, AIP conf. proc., 1000, 581, arXive:astro-ph/0807.0738.

Schmidt, M., 1999, ApJ, 523, L117.

Schmidt, M., 2001a, ApJ, 552, 36.

Schmidt, M., 2001b, ApJ, 559, L79.

Spergel, D.N., Piran, T., Loeb, A., Goodman, J., Bahcall, J.N., 1987, Science, 237, 1471.

Totani, T., 1997, ApJ, 486, L71.

Totani, T., 1999, ApJ, 511, 41.

Ulmer, A., Wijers, R.A.M.J., 1995, ApJ, 439, 303.

Ulmer, A., Wijers, R.A.M.J., Fenimore, E.E., 1995, ApJ, 440, L9.

Wijers, R.M.J., et al. 1998a, MNRAS, 294, L13.

Woosley, S.E., 1993, ApJ, 405, 273.

Yüksel, H., Kistler, M.D., 2007, Phys. Rev. D, 75, 083004.

Yüksel, H., Kistler, M.D., Beacom, J.F., Hopkins, A.M., 2008, ApJ, 683, L5.

APPENDIX A: THE LUMINOSITY

In this work we used only data collected by *Swift*. The peak-flux of each burst, measured in *Swift*'s BAT detectors band 15keV - 150keV (Barthelmy et al. 2005). For most of the bursts we cannot estimate the luminosity in the full γ-range (1keV - 10MeV) as the spectral shape (the Band-function) (Band et al. 1993) is poorly known. We still need however to have some quantitative measure of the luminosity that will be defined uniformly for all burst with a known redshift. To do so we use an average characteristic Band function, $E_{peak} = 511keV$ (in source frame), $\alpha = -1$, $\beta = -2.25$ (Preece et al. 2000; Porciani and Madau 2001) to estimate luminosity, using the same parameters for all bursts, thus the estimated luminosity is proportional to the measured $peak\ flux$ (p):

$$L_{iso} = p4\pi D(z)^2(1+z)k(z)C_{det} \ , \tag{A.1}$$

$D(z)$ is the proper distance at redshift z, C_{det}^{-1} is the fraction of the total $\gamma - ray$ luminosity detected in the detectors energy band for source at redshift = 0,

$$C_{det} = \frac{\int_{1keV}^{10MeV} EN(E)dE}{\int_{E_{min}}^{E_{max}} N(E)dE} , \tag{A.2}$$

$k(z)$ is the k-correction for the given spectrum at redshift z,

$$k(z) = \frac{\int_{E_{min}}^{E_{max}} N(E)dE}{\int_{(1+z)E_{min}}^{(1+z)E_{max}} N(E)dE} , \tag{A.3}$$

where $N(E)$ is the Band function, $E_{min} = 15keV$, $E_{min} = 150keV$. The values in this paper are the luminosity in the range [1keV - 10MeV].

APPENDIX B: THE REDSHIFT DETECTION PROBABILITY

We examine now the redshift detection probability as a function of the $peak\ flux$. We consider here two effects: first the probability to detect the GRB, and second the probability to measure the redshift, for a given detected burst.

The probabilities to detect a GRB, or to measure a redshift, are a function of the burst energy, its duration, and other factors, as described by (Band 2006). We restrict ourselves here only to the dependence of these probabilities in the $peak\ flux$, since this is the quantity we use for the analysis in this paper.

B1 GRB Detection Probability

The simplest model often used is of a sharp threshold: No detection with $p < p_{lim}$, but 100% detection of bursts with $p \geqslant p_{lim}$. For this model the value used at *Swift*'s main detection band $[15 - 150]keV$ is $p_{lim} = 0.4ph/cm^2/sec$. (see Guetta and Piran (2007), Gorosabel et al. (2004)). In the plot of the accumulated number of bursts as a function of $log(p)$, a linear relation appears for fluxes that are low or medium but above the threshold mentioned above. Although we do not try to give a theoretical explanation for this result, we do not expect, however any strong deviation from that connection for lower fluxes, since our models predict a slow gradual smooth change in $dN/dlog(p)$, and we can adopt this values at least as an order of magnitude estimators, to yield a continues threshold estimation. Assuming that the deviation from linearity for fluxes below p_{lim} is only due to a lowered detection sensitivity, we can extrapolate the predicted number of bursts for lower fluxes, and extract the detection sensitivity by comparing the number of detected bursts to the predicted number. Figure B1 shows this: accumulated number of bursts vs. log peak flux, the

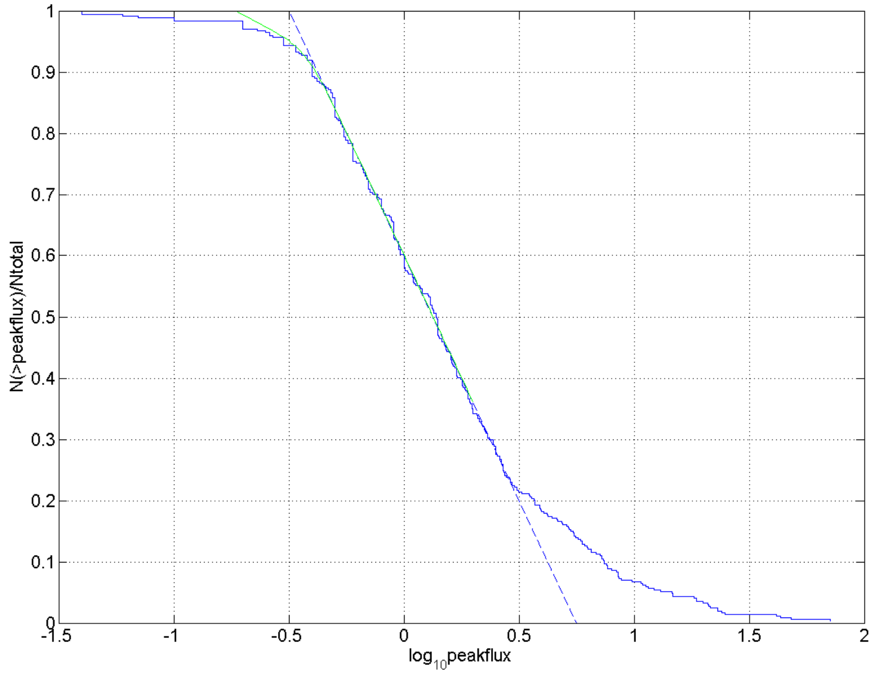

Figure B1. The accumulated number of bursts as function of log(peak flux)

linear fit, and our fit.

$$\theta_\gamma(p) = \begin{cases} \frac{(1+c)}{2} + \frac{(1-c)}{2} erf(d \cdot log(p/p_0) & 0.2 \leqslant p \, , \\ 0 & p < 0.2 \, , \end{cases} \tag{B.1}$$

with the parameters found:

$$c = 0.25, d = 10, log_{10} p_0 = -0.42 \, .$$

B1.1 Redshift Measuring Probability

Redshifts are measured only for a moderate fraction of the detected bursts. A few (5-10%) are too weak, some don't have a clear redshift signature, and some are not measured because of lack of observational resources.

When we consider the fraction of redshift-measured GRBs to the total number of GRBs detected, we see a trend of increase in this fraction with the measured peak number flux of photons in the detectors main band: $15keV - 150keV$, p (see figure B2). We used a linear regression to approximate the relation:

$$\theta_z(p)/\theta_\gamma(p) = a \cdot log(p) + b \, , \tag{B.2}$$

Where , $\theta_\gamma(p)$ is the detection probability, and $\theta_z(p)$ is the probability that a redshift will be mea-

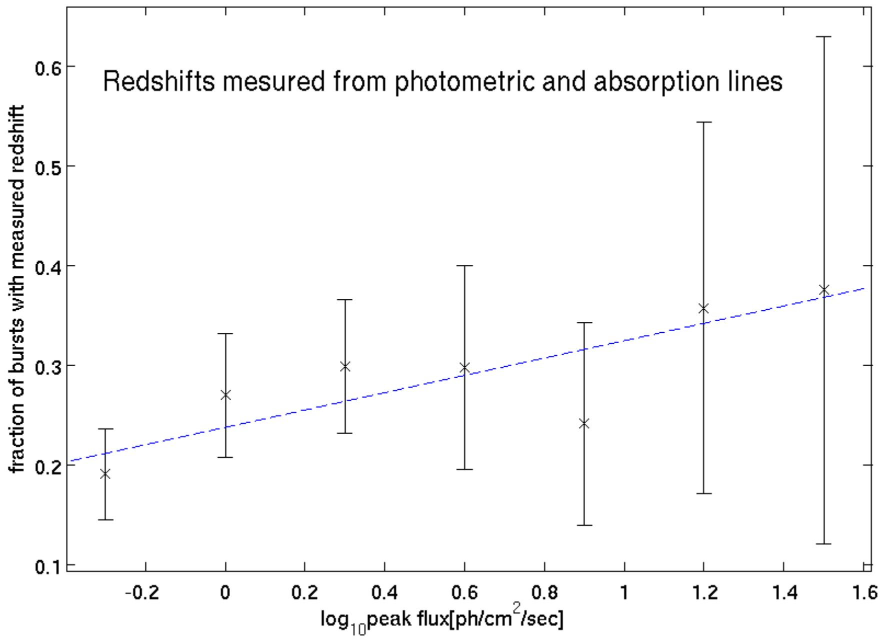

Figure B2. The fraction of bursts with a measured absorption lines and photometry redshift, as function of log(p)

sured. The parameters found in fit are: $a = 0.080 \pm 0.078$ and $b = 0.242 \pm 0.054$. with $\chi^2 = 1.01$ at 5 degrees of freedom, giving a rejection probability of 0.038 . We expect the fraction of number of bursts with redshift $N_z(p)$ to the overall number of bursts $N_\gamma(p)$, for any given p, to obey the relation:

$$\frac{\theta_z(p)}{\theta_\gamma(p)} = \frac{N_z(p)}{N_\gamma(p)} \; . \tag{B.3}$$

Figure B2. depicts the fraction of bursts with a measured redshift and the linear fit, for the absorption and photometry redshifts. Although the fit is acceptable the significant of the effect is just one standard deviation (σ) - so with the current observations the option of no dependence of redshift detection probability with peak flux $(a = 0)$ is still marginally consistent.

Whereas the detection fraction can be fitted well with a linear model for the redshifts obtained using absorption lines, the case is different when considering redshifts obtained using emission lines. Figure B3. shows the measured redshift fraction and the linear fit for the emission lines redshifts. The emission lines redshifts are obtained preferably for high flux bursts, but very few are obtained for low and medium fluxes: 24% for $log_{10}p > 1$, and only 6.5% for $log_{10}p \leqslant 1$. This feature of the emission lines redshifts is associated with a strong bias toward lower redshifts as shown on Figure 1. These results supports our approach of selecting only the absorption lines and photometry redshifts as it make a sample which is less biased and easier to model.

The product of the above probabilities for burst detection and redshift measurement, gives the

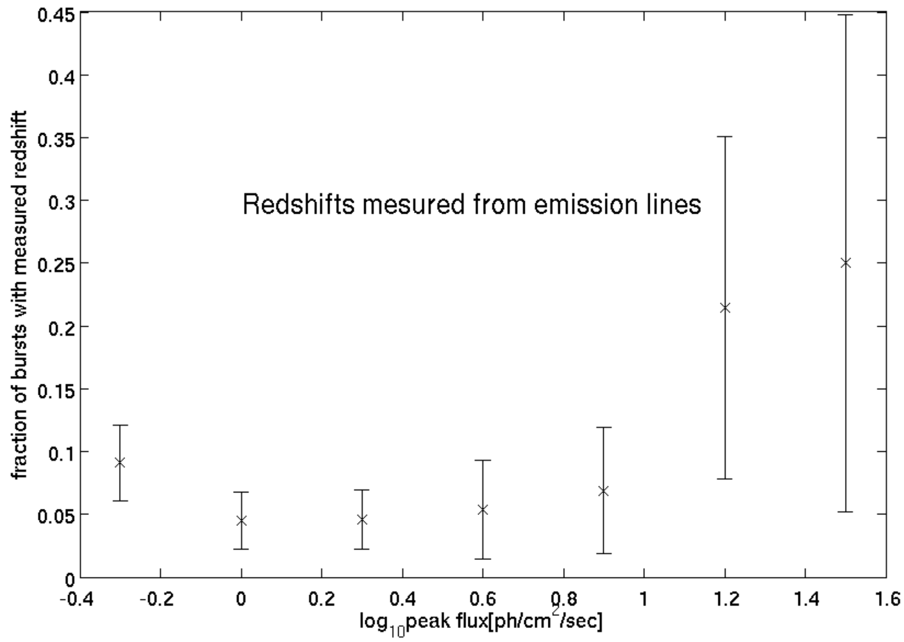

Figure B3. The fraction of bursts with a measured emission lines redshift, as function of log(p)

Prob. z	Prob. γ	$L*$	α	β	z_1	n_1	n_2
-	-	52.54	0.17	1.32	3.13	1.85	-1.38
-	+	52.53	0.04	1.32	2.25	1.53	-0.00
+	-	52.53	0.30	1.44	3.08	2.28	-1.06
+	+	52.53	0.17	1.44	3.11	2.07	-1.36

Table B1. Model's best-fit parameters when taking (+) and when not taking (-) each effect into account.

total probability that we detect a burst and measure its redshift θ_z. Figure B4, shows the function θ_z, which have the form:

$$\theta_z(p) = \begin{cases} (alog(p)+b)(\frac{(1+c)}{2} + \frac{(1-c)}{2} erf(d \cdot log(p/p_0)) & 0.2 \leqslant p \ , \\ 0 & p < 0.2 \ , \end{cases} \tag{B.4}$$

with

$$a = 0.08, b = 0.242, c = 0.25, d = 10, log_{10}p_0 = -0.42 \ .$$

To check the effects of the burst detection probability and the redshift measurement probability, we repeated the process described in this paper, with all four options of taking or not taking into account each of the modified probabilities. The best fit results for the parameters are shown in table B1. For both corrections, we find a non-negligible effect on the results, although the deviations induced on the parameters are in most cases within the statistical error ranges of the analysis.

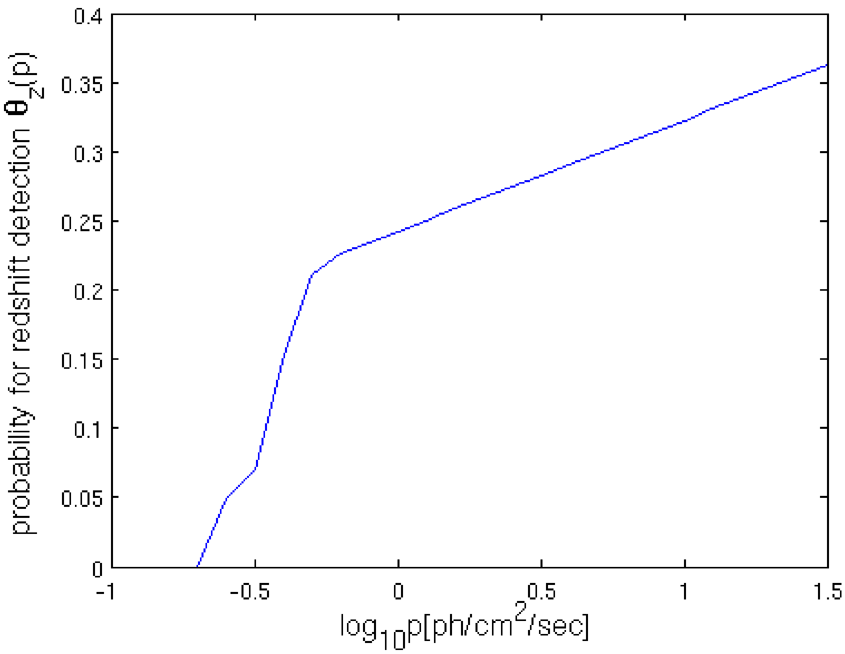

Figure B4. the probability for measuring redshift by absorption lines or by photometry θ_z, as a function of log(peak flux)

When taking both effects into account, the models give somewhat better results in the various statistical tests. Therefor, the function $\theta_z(p)$ that take both effects into account is used in this work.